

Plaquette Singlet Transition, Magnetic Barocaloric Effect, and Spin Supersolidity in the Shastry-Sutherland Model

Junsen Wang,^{1,2,*} Han Li,^{3,4,*} Ning Xi,² Yuan Gao,^{5,2} Qing-Bo Yan,^{1,†} Wei Li,^{2,4,‡} and Gang Su^{3,4,§}

¹Center of Materials Science and Optoelectronics Engineering,

College of Materials Science and Opto-electronic Technology,

University of Chinese Academy of Sciences, Beijing 100049, China.

²CAS Key Laboratory of Theoretical Physics, Institute of Theoretical Physics, Chinese Academy of Sciences, Beijing 100190, China

³Kavli Institute for Theoretical Sciences, University of Chinese Academy of Sciences, Beijing 100190, China

⁴CAS Center for Excellence in Topological Quantum Computation,

University of Chinese Academy of Sciences, Beijing 100190, China

⁵School of Physics, Beihang University, Beijing 100191, China

(Dated: February 28, 2023)

Inspired by recent experimental measurements [Guo *et al.*, Phys. Rev. Lett. **124**, 206602 (2020); Jiménez *et al.*, Nature **592**, 370 (2021)] on frustrated quantum magnet SrCu₂(BO₃)₂ under combined pressure and magnetic fields, we study the related spin-1/2 Shastry-Sutherland (SS) model using state-of-the-art tensor network methods. By calculating thermodynamics, correlations and susceptibilities, we find, in zero magnetic field, not only a line of first-order plaquette-singlet (PS) to dimer-singlet phase transition ending with a critical point, but also signatures of the ordered PS transition with its critical endpoint terminating on this first-order line. Moreover, we uncover prominent magnetic barocaloric responses, a novel type of quantum correlation induced cooling effect, in the strongly fluctuating supercritical regime. Under finite fields, we identify a quantum phase transition from the PS phase to the spin supersolid phase that breaks simultaneously lattice translational and spin rotational symmetries. The present findings on the SS model are accessible in current experiments and would shed new light on exotic critical and supercritical phenomena in archetypal frustrated quantum magnets.

Introduction.— Frustrated magnetism constitutes a fertile ground breeding enriched spin states and phase transitions [1, 2], including unusual spin orders, quantum spin liquid (QSL) [3–5], and unconventional quantum critical point (QCP) like the deconfined QCP (DQCP) [6], etc. The paradigmatic Shastry-Sutherland (SS) model is a highly frustrated quantum spin system with an analytically known ground state in certain parameter regime [7]. Nevertheless, its global phase diagram hosts rich spin states and transitions, where numerical simulations are playing an increasingly important role [8–25]. On the other hand and as a miracle of nature, the SS model is faithfully realized by a quantum magnetic material SrCu₂(BO₃)₂ whose pressure-field-temperature phase diagram is under intensive investigation [26–34], and the intriguing magnetic phenomena observed in experiments in turn requires further theoretical studies of the SS model.

The spin-1/2 SS model is defined on a square lattice with the Hamiltonian

$$H = J \sum_{\langle i,j \rangle} \mathbf{S}_i \cdot \mathbf{S}_j + J' \sum_{\langle\langle i,j \rangle\rangle} \mathbf{S}_i \cdot \mathbf{S}_j, \quad (1)$$

where $J > 0$ is the antiferromagnetic (AF) coupling on the inter-dimer, and $J' > 0$ on the intra-dimer bonds [c.f., Fig. 1(b)]. We take $J' = 1$ as the energy scale hereafter. For $\alpha \equiv J/J' \leq 0.5$, the ground state is rigorously a product of singlets on the J' dimers [7], dubbed the dimer-singlet (DS) phase. While for the other limit, $\alpha \gg 1$, it has clearly a Néel AF state [35], and possible intermediate phases were debated for decades [8–17]. Now consensus has more or less reached that there exists an intervening plaquette-singlet (PS) phase [18–25, 28, 30, 32, 33]. The DS-PS transition is first-order, while the PS-AF transition is possibly second-order and

belongs to a DQCP [20]. Evidence of the intermediate PS phase and pressure-induced quantum phase transitions (QPTs) were indeed found in recent experiments [28, 30, 31]

However, there are still enigmas surrounding this seemingly innocent PS phase. For example, recent ground-state studies suggest that the plaquette singlets sit on “empty” plaquettes without diagonal bonds [18, 20–25], while experiments show that they instead sit on “full” plaquettes containing diagonal bonds [28, 32, 37]. An intriguing question within the minimal SS model therefore arises: How about the competition between the instabilities towards empty/full PS order *at finite temperature*? Recent specific heat measurements on SrCu₂(BO₃)₂ found a signal at $T \sim 2$ K, conjecturing that it reflects the onset of PS order [30, 31]. Despite of great efforts for thermodynamics simulations made in recent years [21, 38, 39], this signal remains illusive theoretically due to the great challenges in unbiased calculations down to low temperature.

In this work, we perform a finite-temperature study of the SS model on a cylinder geometry with the state-of-the-art exponential tensor renormalization group (XTRG) approach [40–42]. XTRG has been successfully used in studying frustrated quantum magnets [43–46], and here we simulate the SS model down to $T/J' \sim 0.006$ on a long cylinder. By mapping out the phase diagram, we reproduce the critical point [31] and uncover the empty PS phase below the thermal transition line T_P^* with a \mathbb{Z}_2 symmetry breaking. Although the calculations are restricted within $W = 6$ cylinders, we believe the conclusions also hold for wider cylinders, and therefore explain the specific heat peak observed at $T \lesssim 2$ K in recent experiments [30, 31]. We further propose a pronounced adiabatic quantum spin cooling effect driven by pressure (that

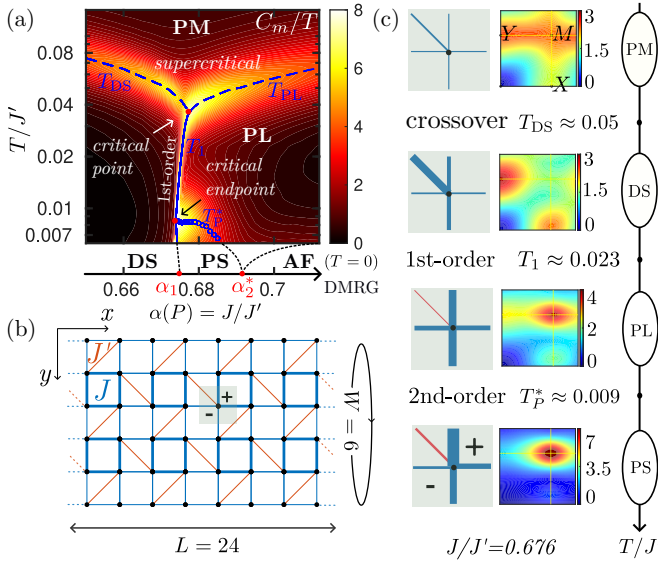


FIG. 1. (a) Pressure-temperature phase diagram of the SS model with magnetic specific heat C_m/T as contour background. The low-temperature data smoothly extrapolate to the ground-state results, where a first-order QPT occurring at $\alpha_1 \simeq 0.673$ and a QCP at $\alpha_c^* \simeq 0.692$ are obtained by DMRG [36] on the same geometry. Two crossovers T_{DS} and T_{PL} (blue dashed lines), first-order T_1 (solid line), and second-order transition T_P^* (empty circle for each data point) are determined from peaks of C_m/T . (b) The 6×24 cylinder with the ordered PS phase illustrated. (c) Temperature evolution of local bond correlators (first column), static spin structure factors (second column) and the corresponding phases (third column) for $J/J' = 0.676$. Local correlators are measured at the center of the lattice, exemplified by the light green square in (b), with two types of empty plaquettes indicated by $+$ and $-$ signs, respectively. Blue (red) bonds indicate negative (positive) correlations with their widths proportional to the absolute values.

controls the coupling ratio α) in the supercritical regime. As a companion, we also perform density-matrix renormalization group (DMRG) [47] calculations to explore the QPTs driven by combined pressure and magnetic fields. In particular, evidence for the QPT between the PS phase and a spin super-solid (SSS) phase is witnessed, whose location quantitatively agrees with recent experiments [32].

The SS model phase diagram.— The obtained pressure-temperature phase diagram of the SS model is shown in Fig. 1(a) based on the contour plot of the magnetic specific heat C_m/T . As the first-order transition line is slightly bent, one goes over various spin states as temperature decreases with fixed $J/J' = 0.676$, and find in Fig. 1(c) intriguing temperature-evolution behaviors: Starting from the high- T paramagnetic (PM) phase, the system evolves into the DS regime [second row of Fig. 1(c)], where the intra-dimer correlation $C_D = -\langle \mathbf{S}_i \cdot \mathbf{S}_j \rangle_D$ [c.f., inset in Fig. 2(c)] is strongest and the spin structure factor peaks at X and Y points in the first Brillouin zone. Further decreasing temperature, it enters the plaquette liquid (PL) phase via a first-order transition, where C_D changes its sign and the inter-dimer corre-

lation $C_{NN} = -\langle \mathbf{S}_i \cdot \mathbf{S}_j \rangle_{NN}$ [see also inset in Fig. 2(c)] becomes stronger, as shown in the third row of Fig. 1(c). In the PM, DS, and PL regimes, the equivalent NN bonds take the same values and there is no \mathbb{Z}_2 symmetry breaking; while at sufficiently low temperatures ($T < T_P^*$), the PL phase eventually gives way to the ordered PS phase upon a second-order transition. The PS order can be detected by comparing two bonds with the same orientation [48], as shown in the last row of Fig. 1(c). Correspondingly, the spin structure peak shifts to the M point in the PL and ordered PS phases, with the latter being brighter. Markedly, this interesting temperature evolution of spin states due to the slightly bent first-order line is consistent with the results in a recent NMR experiment, where a phase coexistence phenomenon was observed [32].

First-order line and critical point.— We determine the critical point (CP), $(\alpha_c^*, T_c^*/J') \simeq (0.678, 0.036)$, in Fig. 1(a) as the position where two dashed lines, T_{DS} and T_{PL} , and the solid line T_1 meet. The latter, i.e., a first-order transition line, can be understood from intra-dimer correlation C_D , which serves as the corresponding density-type order parameter. As shown in Fig. 2(a), for $T < T_c^*$, a discontinuous jump in C_D occurs at $\alpha_1 \simeq 0.675$, a characteristic of the first-order transition between the DS and PL/PS phase. In contrast, for $T > T_c^*$, the simulated C_D data show a smooth change, which resembles that of liquid-gas crossover in the supercritical regime of water's pressure-temperature phase diagram [31]. According to the couplings determined in Refs. [28, 30], our results correspond to a critical pressure around 2 GPa, and a critical temperature T_c^* about 2-3 K, in agreements with recent experiments [31]. We further examine the correlation jump between the DS and PS states $\Delta C_D \sim (\frac{T_c^* - T}{T_c^*})^\beta$ near the CP (from below) [31], with the fitted critical exponent $\beta \approx 1/8$ [36] falling into the two-dimensional Ising universality class. Notably, the white line in Fig. 2(a) with $C_D \approx 0$, roughly coincides with the T_{PL} line and indicate a *sign-switching* in the intra-dimer correlations, which has been observed experimentally [37].

In Fig. 1(a), there are two crossover temperature scales, T_{DS} and T_{PL} , determined from C_m/T humps. They can be elucidated by examining two types of local correlations, i.e., the inter-dimer C_{NN} and the intra-dimer C_D . As shown in Fig. 2(c) and (d), a shoulder-like structure is firstly developed in C_m/T at $T_h \sim 0.4J'$, where both correlations build up with similar strengths. However, it is found that for $\alpha = 0.67 < \alpha_1$, [c.f., Fig. 2(c)], the intra-(inter-) dimer correlations increase (decrease) rapidly around T_{DS} ; while, for $\alpha = 0.68 > \alpha_1$, [c.f., Fig. 2(d)], the situation around T_{PL} is reversed. Moreover, we note that the empty PS order parameter \mathcal{O}_E , defined in the inset of Fig. 2(c), remains vanishingly small till T_P^* , indicating the fluctuating plaquette order in the PL regime yet without \mathbb{Z}_2 symmetry breaking.

Second-order line and critical endpoint.— When further decreasing temperature, the specific heat peak gets brighter and becomes maximal at $(\alpha_E, T_E/J') \approx (0.674, 0.008)$, as shown in Fig. 1(a), which is nothing but the critical end-

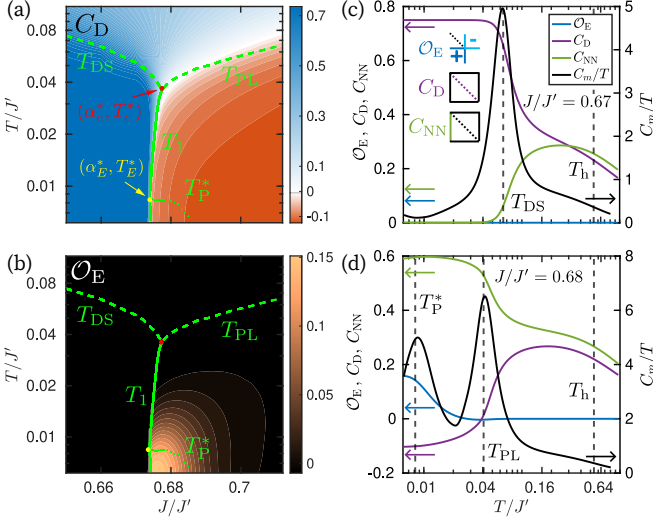


FIG. 2. Contour plots of (a) intra-dimer correlator C_D and (b) order parameter $O_E \equiv \sum_i [(-1)^{i_x} \mathbf{S}_i \cdot \mathbf{S}_{i+\hat{x}} - (-1)^{i_y} \mathbf{S}_i \cdot \mathbf{S}_{i+\hat{y}}]$ for the empty PS order. Green dashed, solid, and dotted lines are peaks of C_m/T , and red (yellow) dot represents the CP (CEP) [c.f. Fig. 1(a)]. (c)-(d) Magnetic specific heat C_m/T , in conjunction with C_D , inter-dimer correlator C_{NN} , and O_E v.s. T , for $J/J' = 0.67$ and 0.68 , respectively. The inset in (c) illustrates definitions of these quantities. Roughly 6% total entropy is released near the T_P^* peak, consistent with experimental result of $\sim 4\%$ obtained at 1.8 GPa [30].

point (CEP) [49, 50]. On the right hand side of this point, there is a second-order thermal transition line T_P^* defined by the peaks of C_m/T , which goes downwards and eventually drops outside of our temperature window when approaching the possible QPT at $\alpha_2^* \approx 0.692$ determined by DMRG calculations [36]. Such a peak structure has been experimentally observed recently [30, 31]. Here we perform low-temperature calculations down to previously inaccessible regime [21, 31, 38, 39], and identify the ordered PS phase below the transition temperature $T_P^* \sim 0.01J'$, i.e., resembling the “solid” or “ice” beneath the “liquid” phase in the water’s phase diagram. The low-temperature calculations smoothly extrapolate to the ground-state DMRG results, and hence provide a *comprehensive* pressure-temperature phase diagram of the SS model in Fig. 1(a).

One major mystery of the SS model and $\text{SrCu}_2(\text{BO}_3)_2$ is the nature of the low-temperature PS phase, i.e., whether the \mathbb{Z}_2 symmetry breaking occurs among the empty or full plaquettes. Recent experiments on $\text{SrCu}_2(\text{BO}_3)_2$ [28, 32, 37] suggest the latter while numerics support the former [18, 20–25]. To characterize this symmetry-breaking PS phase, we compute order parameters for both the empty (O_E) and full (O_F) PS states. The former is shown in Figs. 2, while the latter is found to be much smaller [36]. In Fig. 2(d), we find O_E remains zero until around T_P^* , where the specific heat shows a peak. It corresponds to the rapid buildup of \mathbb{Z}_2 symmetry breaking order amongst empty plaquettes. We also compute the PS susceptibility for both empty (χ_E) and full (χ_F) PS

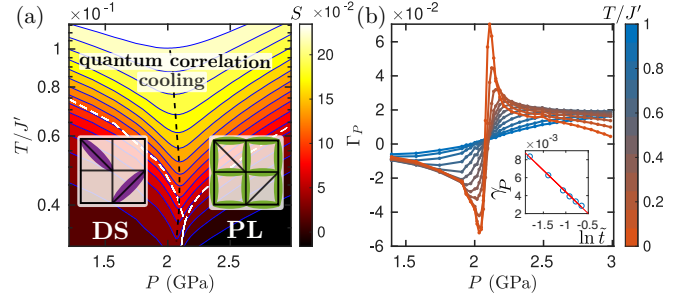


FIG. 3. (a) Contour plot of thermal entropy S with isentropes indicated by black solid lines, where prominent cooling effect due to dramatic change in quantum correlations is observed. The white dashed and solid lines are determined from C_m/T [c.f., Fig. 1(a)]. The black dashed line connects the dips of isentropes and represents a line of maximal entropy. (b) Grüneisen ratio Γ_P vs. pressure P . The inset shows $\gamma_P(\tilde{t})$ v.s. $\ln \tilde{t} \equiv \ln[(T - T_c^*)/T_c^*]$ (blue circles), with the fitting (red line) also shown. In both panels, we use the relation between coupling strength and pressure given by [28], i.e., $J'(P) = (75 - 8.3P/\text{GPa})\text{K}$ and $J(P) = (46.7 - 3.7P/\text{GPa})\text{K}$.

orders, and find that the former increases much faster in the PL regime below T_{PL} [36]. Therefore, we conclude that the empty PS instability predominates over the full one in the entire low-temperature range, and confirm that the PS phase is of empty-type in the pressure-temperature phase diagram.

Supercritical regime and magnetic barocalorics.— It is well-known that water in its supercritical state has many fascinating physical properties leading to various applications [51]. In the case of quantum magnets, the supercritical regime remains largely unexplored [52]. Here we initiate the investigation of supercriticality in the SS model from the perspective of magnetothermodynamics. In Fig. 3(a), we present the isentropes in this regime, where a very prominent adiabatic magnetic cooling effect is found. By connecting the lowest temperature points of isentropes, we obtain a maximal entropy line with strong spin fluctuations that resembles the renowned Widom line [53]. As such prominent cooling effect originates from magnetic entropy and is controlled by pressure, we dub it *magnetic barocaloric effect* (mBCE), and propose to characterize it by a Grüneisen ratio $\Gamma_P \equiv -\frac{1}{T} \frac{(\partial S/\partial P)_T}{(\partial S/\partial T)_P}$. As shown in Fig. 3(b), a clear sign change with very pronounced peak/dip can be observed in Γ_P for supercritical spin states. More specifically, we denote the nominator by $\gamma_P \equiv -(\partial S/\partial P)_T \sim \partial \langle \mathbf{S}_i \cdot \mathbf{S}_j \rangle / \partial T$, and find a universal scaling $\gamma_P \sim \ln[(T - T_c^*)/T_c^*]$ near the CP [c.f., the inset of Fig. 3(b)], dictated by the 2D Ising universality class. Notably, in sharp distinction to the conventional magnetic cooling due to entropy change in order-disorder reorientations of magnetic moments [54], here the mBCE originates from the rearrangements in spin singlet patterns [illustrated in the inset of Fig. 3(a)]. Such a quantum correlation induced cooling, observed in the supercritical regime and below, occurs between two magnetically disordered states and constitutes a novel mechanism for helium-free cryogenics.

Field-temperature phase diagram and spin-supersolid

transition.— Given the ordered PS phase identified, we consider applying magnetic fields to pressured $\text{SrCu}_2(\text{BO}_3)_2$ [32, 33] along the z direction, i.e., $H \rightarrow H - h \sum_i S_i^z$. Here we focus on $J/J' = 0.68$ and $h/J' \leq 0.25$, and the contour plot of C_m/T is shown in Fig. 4(a), where we find both temperature scales, T_{PL} and T_{P}^* , decrease as the field increases, and the latter will eventually drop out of our temperature window. A low-temperature C_m/T peak reappears for $h/J' \gtrsim 0.22$, suggesting a QPT occurs before $h/J' = 0.22$.

To clarify the quantum phases and phase transitions in Fig. 4(a), we perform DMRG calculations and show the results in Figs. 4(b) and (c). On width-6 cylinder, there exists an pressure-induced intermediate PS phase [20], which gives way to a stripy SSS [33] phase for $h > h_c/J' \simeq 0.185$ [c.f., Fig. 4(b)] via a QPT possibly of first order [36]. In the SSS phase with $h/J' = 0.2$, we show the computed local moments in Fig. 4(c) where a 10×2 unit cell can be observed, similar to the previously iPEPS results [33]. In the SSS phase, both $\langle M_x \rangle$ and $\langle M_z \rangle$ are nonzero, indicating that both translational and U(1) symmetries are simultaneously broken, i.e., there exists a quantum magnetic analogue of supersolidity. Taking $J' \approx 60$ K for $\text{SrCu}_2(\text{BO}_3)_2$ under pressure of about 2.0 GPa [30], we estimate the field-driven QPT takes place at $h_c \approx 8$ T, in agreement with recent experiments [32, 33].

The SSS order is also evident in the spin structure factors $S^{\gamma\gamma}(\mathbf{k}) = N^{-1} \sum_{i,j} e^{-i\mathbf{k} \cdot (\mathbf{r}_i - \mathbf{r}_j)} \langle S_i^\gamma \cdot S_j^\gamma \rangle$ (with N the total lattice sites) shown in the insets of Fig. 4(b), where a broad peak in the PS phase changes into a double-peak structure split apart at $k_x = \pi \pm \frac{\pi}{5}$, as h changes from 0.16 to 0.2. Such a peak-splitting behavior is also found when decreasing temperature [36], accessible by neutron scattering measurements for probing the SSS phase. We note that for different choices of α , other phases may show up instead of SSS, making the field-driven spin states and transitions extremely rich in pressured $\text{SrCu}_2(\text{BO}_3)_2$ [32, 33].

Discussion and outlook.— Recent experimental advances [30–32] have added greatly to the understanding of the pressure-field-temperature phase diagram of $\text{SrCu}_2(\text{BO}_3)_2$, which advocate comprehensive theoretical studies in particular at finite temperature. Here with state-of-the-art tensor-network approach, we map out the phase diagram that explains experimental findings and opens a refreshing avenue in the $\text{SrCu}_2(\text{BO}_3)_2$ studies. In particular, the order PS phase and its thermal transition line are identified, and the controversy on nature of the PS phase is clarified by finding that the empty PS order is predominant over the full one below $T/J' \sim 0.01$. Moreover, we call for future experimental investigations of the magnetic barocalorics in the supercritical regime, which constitutes a *bona fide* spin correlation cooling effect fundamentally different from traditional magnetic refrigeration. The novel cooling mechanism in frustrated magnets enables potential applications in space cryogenics [55] and quantum technologies [56].

The pressure-driven PS-AF quantum phase transition has intensively studied recently [20, 24, 25]. Our finite- T studies here find no salient feature near α_2^* in simulated quan-

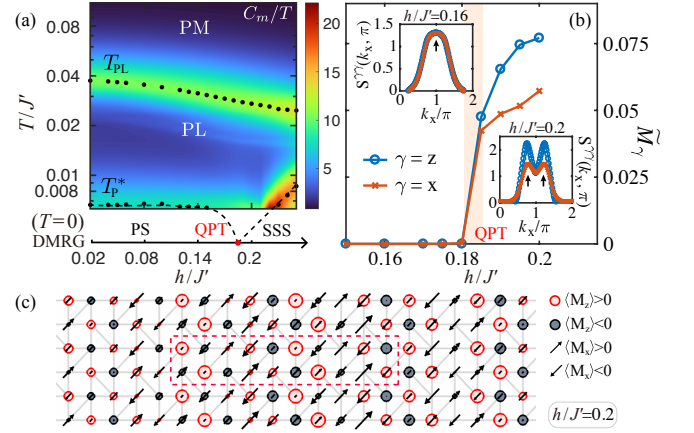


FIG. 4. (a) Contour plot of C_m/T with black dots indicating locations of the peaks, which extrapolate to the ground-state phase diagram where a QPT occurs at $h_c/J' \simeq 0.185$ (with $J/J' = 0.68$). (b) The “solid” and “superfluid” spin order parameters \tilde{M}_γ ($\gamma = x, z$) computed as $\frac{1}{N_{\text{Bulk}}} \sum_{i \in \text{Bulk}} |\langle M_\gamma \rangle_i|$ with site i running over bulk of the cylinder. The insets show the spin-structure factors $S^{zz}(k_x, k_y)$ and $S^{xx}(k_x, k_y)$, under two different fields $h/J' = 0.16$ and 0.2 . (c) Spin texture in the SSS phase, where the moments are displayed with the longitudinal ($\langle M_z \rangle_i$) and transverse ($\langle M_x \rangle_i$) magnetic moments. The positive (negative) $\langle M_z \rangle_i$ values are illustrated with red (black) circles, and the $\langle M_x \rangle_i$ components with the arrows. Size of circles and length of arrows reflect the absolute values of corresponding order parameters, where a 10×2 unit cell on a 6×30 cylinder is indicated by the red dashed box.

ties [36], which might be ascribed to the limited width-6 cylinder used in the calculations. Whether this transition belongs to a DQCP [20] or is replaced by a QSL phase [23–25] unfortunately can not be addressed here. Instead, the field-driven PS-SSS transition in the case of $\alpha = 0.68$ (i.e., under 2.2 GPa pressure) belongs to first order and can be clearly signalled by magnetocaloric measurements [36]. Meanwhile, a field-driven PS-AF phase transition was recently observed under a relatively higher pressure (e.g., 2.4 GPa) and has been suggested to be a proximate DQCP [32], which remains for future studies.

Acknowledgments.— J.W. and W.L. are indebted to Rong Yu, Ling Wang, Anders Sandvik, Zi Yang Meng, and Weiqiang Yu for stimulating discussions. This work was supported by the National Natural Science Foundation of China (Grant Nos. 12222412, 11834014, 11974036, and 12047503), National Key R&D Program of China (Grant Nos. 2018YFA0305800 and 2022YFA1402704), Strategic Priority Research Program of Chinese Academy of Sciences (CAS) (Grant No. XDB 28000000), the CAS Project for Young Scientists in Basic Research (YSBR-003, YSBR-057), and the Fundamental Research Funds for the Central Universities. We thank the HPC-ITP for the technical support and generous allocation of CPU time.

* These authors contributed equally to this work.

† yan@ucas.ac.cn

‡ w.li@itp.ac.cn

§ gsu@ucas.ac.cn

- [1] C. Lacroix, P. Mendels, and F. Mila, eds., *Introduction to Frustrated Magnetism* (Springer Berlin Heidelberg, 2011).
- [2] H. T. Diep, *Frustrated Spin Systems*, 3rd ed. (World Scientific, 2020).
- [3] L. Balents, Spin liquids in frustrated magnets, *Nature* **464**, 199 (2010).
- [4] Y. Zhou, K. Kanoda, and T.-K. Ng, Quantum spin liquid states, *Rev. Mod. Phys.* **89**, 025003 (2017).
- [5] C. Broholm, R. J. Cava, S. A. Kivelson, D. G. Nocera, M. R. Norman, and T. Senthil, Quantum spin liquids, *Science* **367**, eaay0668 (2020).
- [6] T. Senthil, A. Vishwanath, L. Balents, S. Sachdev, and M. P. A. Fisher, Deconfined quantum critical points, *Science* **303**, 1490 (2004).
- [7] B. S. Shastry and B. Sutherland, Exact ground state of a quantum mechanical antiferromagnet, *Physica B+C* **108**, 1069 (1981).
- [8] M. Albrecht and F. Mila, First-order transition between magnetic order and valence bond order in a 2D frustrated Heisenberg model, *Europhysics Letters (EPL)* **34**, 145 (1996).
- [9] S. Miyahara and K. Ueda, Exact dimer ground state of the two dimensional Heisenberg spin system $\text{SrCu}_2(\text{BO}_3)_2$, *Phys. Rev. Lett.* **82**, 3701 (1999).
- [10] E. Müller-Hartmann, R. R. P. Singh, C. Knetter, and G. S. Uhrig, Exact Demonstration of Magnetization Plateaus and First-Order Dimer-Néel Phase Transitions in a Modified Shastry-Sutherland Model for $\text{SrCu}_2(\text{BO}_3)_2$, *Phys. Rev. Lett.* **84**, 1808 (2000).
- [11] A. Koga and N. Kawakami, Quantum phase transitions in the Shastry-Sutherland model for $\text{SrCu}_2(\text{BO}_3)_2$, *Phys. Rev. Lett.* **84**, 4461 (2000).
- [12] W. Zheng, J. Oitmaa, and C. J. Hamer, Phase diagram of the Shastry-Sutherland antiferromagnet, *Phys. Rev. B* **65**, 014408 (2001).
- [13] Y. Takushima, A. Koga, and N. Kawakami, Competing spin-gap phases in a frustrated quantum spin system in two dimensions, *J. Phys. Soc. Jpn.* **70**, 1369 (2001).
- [14] C. H. Chung, J. B. Marston, and S. Sachdev, Quantum phases of the Shastry-Sutherland antiferromagnet: Application to $\text{SrCu}_2(\text{BO}_3)_2$, *Phys. Rev. B* **64**, 134407 (2001).
- [15] A. Läuchli, S. Wessel, and M. Sigrist, Phase diagram of the quadrumerized Shastry-Sutherland model, *Phys. Rev. B* **66**, 014401 (2002).
- [16] A. Isacsson and O. F. Syljuåsen, Variational treatment of the Shastry-Sutherland antiferromagnet using projected entangled pair states, *Phys. Rev. E* **74**, 026701 (2006).
- [17] J. Lou, T. Suzuki, K. Harada, and N. Kawashima, Study of the Shastry Sutherland model using multi-scale entanglement renormalization ansatz, *1212.1999v1*.
- [18] P. Corboz and F. Mila, Tensor network study of the Shastry-Sutherland model in zero magnetic field, *Phys. Rev. B* **87**, 115144 (2013).
- [19] C. Boos, S. P. G. Crone, I. A. Niesen, P. Corboz, K. P. Schmidt, and F. Mila, Competition between intermediate plaquette phases in $\text{SrCu}_2(\text{BO}_3)_2$ under pressure, *Phys. Rev. B* **100**, 140413(R) (2019).
- [20] J. Y. Lee, Y.-Z. You, S. Sachdev, and A. Vishwanath, Signatures of a deconfined phase transition on the Shastry-Sutherland lattice: Applications to quantum critical $\text{SrCu}_2(\text{BO}_3)_2$, *Phys. Rev. X* **9**, 041037 (2019).
- [21] T. Shimokawa, Signatures of finite-temperature mirror symmetry breaking in the $S = \frac{1}{2}$ Shastry-Sutherland model, *Phys. Rev. B* **103**, 134419 (2021).
- [22] N. Xi, H. Chen, Z. Y. Xie, and R. Yu, First-order transition between the plaquette valence bond solid and antiferromagnetic phases of the Shastry-Sutherland model, *2111.07368v1*.
- [23] A. Keles and E. Zhao, Rise and fall of plaquette order in the Shastry-Sutherland magnet revealed by pseudofermion functional renormalization group, *Phys. Rev. B* **105**, L041115 (2022).
- [24] L. Wang, Y. Zhang, and A. W. Sandvik, Quantum spin liquid phase in the Shastry-Sutherland model detected by an improved level spectroscopic method, *Chin. Phys. Lett.* **39**, 077502 (2022).
- [25] J. Yang, A. W. Sandvik, and L. Wang, Quantum criticality and spin liquid phase in the Shastry-Sutherland model, *Phys. Rev. B* **105**, L060409 (2022).
- [26] H. Kageyama, K. Yoshimura, R. Stern, N. V. Mushnikov, K. Onizuka, M. Kato, K. Kosuge, C. P. Slichter, T. Goto, and Y. Ueda, Exact dimer ground state and quantized magnetization plateaus in the two-dimensional spin system $\text{SrCu}_2(\text{BO}_3)_2$, *Phys. Rev. Lett.* **82**, 3168 (1999).
- [27] G. Radtke, A. Saúl, H. A. Dabkowska, M. B. Salamon, and M. Jaime, Magnetic nanopantograph in the $\text{SrCu}_2(\text{BO}_3)_2$ Shastry-Sutherland lattice, *Proc. Natl. Acad. Sci.* **112**, 1971 (2015).
- [28] M. E. Zayed, C. Rüegg, J. L. J., A. M. Läuchli, C. Panagopoulos, S. S. Saxena, M. Ellerby, D. F. McMorrow, T. Strässle, S. Klotz, G. Hamel, R. A. Sadykov, V. Pomjakushin, M. Boehm, M. Jiménez-Ruiz, A. Schneidewind, E. Pomjakushina, M. Stingaciu, K. Conder, and H. M. Rønnow, 4-spin plaquette singlet state in the shastry-sutherland compound $\text{SrCu}_2(\text{BO}_3)_2$, *Nat. Phys.* **13**, 962 (2017).
- [29] P. A. McClarty, F. Krüger, T. Guidi, S. F. Parker, K. Refson, A. W. Parker, D. Prabhakaran, and R. Coldea, Topological triplon modes and bound states in a Shastry-Sutherland magnet, *Nat. Phys.* **13**, 736 (2017).
- [30] J. Guo, G. Sun, B. Zhao, L. Wang, W. Hong, V. A. Sidorov, N. Ma, Q. Wu, S. Li, Z. Y. Meng, A. W. Sandvik, and L. Sun, Quantum phases of $\text{SrCu}_2(\text{BO}_3)_2$ from high-pressure thermodynamics, *Phys. Rev. Lett.* **124**, 206602 (2020).
- [31] J. L. Jiménez, S. P. G. Crone, E. Fogh, M. E. Zayed, R. Lortz, E. Pomjakushina, K. Conder, A. M. Läuchli, L. Weber, S. Wessel, A. Honecker, B. Normand, C. Rüegg, P. Corboz, H. M. Rønnow, and F. Mila, A quantum magnetic analogue to the critical point of water, *Nature* **592**, 370 (2021).
- [32] Y. Cui, L. Liu, H. Lin, K.-H. Wu, W. Hong, X. Liu, C. Li, Z. Hu, N. Xi, S. Li, R. Yu, A. W. Sandvik, and W. Yu, Proximate deconfined quantum critical point in $\text{SrCu}_2(\text{BO}_3)_2$, *2204.08133v2*.
- [33] Z. Shi, S. Dissanayake, P. Corboz, W. Steinhart, D. Graf, D. M. Silevitch, H. A. Dabkowska, T. F. Rosenbaum, F. Mila, and S. Haravifard, Discovery of quantum phases in the Shastry-Sutherland compound $\text{SrCu}_2(\text{BO}_3)_2$ under extreme conditions of field and pressure, *Nat. Commun.* **13**, 2301 (2022).
- [34] T. Nomura, P. Corboz, A. Miyata, S. Zherlitsyn, Y. Ishii, Y. Kohama, Y. H. Matsuda, A. Ikeda, C. Zhong, H. Kageyama, and F. Mila, The Shastry-Sutherland compound $\text{SrCu}_2(\text{BO}_3)_2$ studied up to the saturation magnetic field, *2209.07652v1*.
- [35] E. Manousakis, The spin- $\frac{1}{2}$ Heisenberg antiferromagnet on a square lattice and its application to the cuprous oxides, *Rev.*

- Mod. Phys. **63**, 1 (1991).
- [36] See Supplemental Material at [URL will be inserted by publisher], which includes Refs. [14,18,22,25,33,40,41,57-64], for details on (i) finite-temperature tensor renormalization group, (ii) density matrix renormalization group simulations, and more results on the SSM (iii) in zero magnetic field as well as (iv) under finite fields.
- [37] S. Bettler, L. Stoppel, Z. Yan, S. Gvasaliya, and A. Zheludev, Sign switching of dimer correlations in $\text{SrCu}_2(\text{BO}_3)_2$ under hydrostatic pressure, *Phys. Rev. Research* **2**, 012010(R) (2020).
- [38] S. Wessel, I. Niesen, J. Stapmanns, B. Normand, F. Mila, P. Corboz, and A. Honecker, Thermodynamic properties of the Shastry-Sutherland model from quantum monte carlo simulations, *Phys. Rev. B* **98**, 174432 (2018).
- [39] A. Wietek, P. Corboz, S. Wessel, B. Normand, F. Mila, and A. Honecker, Thermodynamic properties of the Shastry-Sutherland model throughout the dimer-product phase, *Phys. Rev. Research* **1**, 033038 (2019).
- [40] B.-B. Chen, Y.-J. Liu, Z. Chen, and W. Li, Series-expansion thermal tensor network approach for quantum lattice models, *Phys. Rev. B* **95**, 161104(R) (2017).
- [41] B.-B. Chen, L. Chen, Z. Chen, W. Li, and A. Weichselbaum, Exponential thermal tensor network approach for quantum lattice models, *Phys. Rev. X* **8**, 031082 (2018).
- [42] H. Li, B.-B. Chen, Z. Chen, J. von Delft, A. Weichselbaum, and W. Li, Thermal tensor renormalization group simulations of square-lattice quantum spin models, *Phys. Rev. B* **100**, 045110 (2019).
- [43] H. Li, Y.-D. Liao, B.-B. Chen, X.-T. Zeng, X.-L. Sheng, Y. Qi, Z. Y. Meng, and W. Li, Kosterlitz-Thouless melting of magnetic order in the triangular quantum Ising material TmMgGaO_4 , *Nat. Commun.* **11**, 1111 (2020).
- [44] H. Li, H.-K. Zhang, J. Wang, H.-Q. Wu, Y. Gao, D.-W. Qu, Z.-X. Liu, S.-S. Gong, and W. Li, Identification of magnetic interactions and high-field quantum spin liquid in $\alpha\text{-RuCl}_3$, *Nat. Commun.* **12**, 4007 (2021).
- [45] S. Yu, Y. Gao, B.-B. Chen, and W. Li, Learning the effective spin Hamiltonian of a quantum magnet, *Chin. Phys. Lett.* **38**, 097502 (2021).
- [46] Y. Gao, Y.-C. Fan, H. Li, F. Yang, X.-T. Zeng, X.-L. Sheng, R. Zhong, Y. Qi, Y. Wan, and W. Li, Spin supersolidity in nearly ideal easy-axis triangular quantum antiferromagnet $\text{Na}_2\text{BaCo}(\text{PO}_4)_2$, *npj Quantum Mater.* **7**, 89 (2022).
- [47] S. R. White, Density matrix formulation for quantum renormalization groups, *Phys. Rev. Lett.* **69**, 2863 (1992).
- [48] The cylinder boundary condition introduces an effective pinning field that may favour a particular plaquette pattern [25], and in practice we measure the order parameters in the central unit cell as elaborated in [36].
- [49] M. E. Fisher and P. J. Upton, Universality and interfaces at critical end points, *Phys. Rev. Lett.* **65**, 2402 (1990).
- [50] M. E. Fisher and M. C. Barbosa, Phase boundaries near critical end points. i. thermodynamics and universality, *Phys. Rev. B* **43**, 11177 (1991).
- [51] A. A. Clifford and J. R. Williams, Introduction to supercritical fluids and their applications, in *Supercritical Fluid Methods and Protocols*, edited by J. R. Williams and A. A. Clifford (Humana Press, Totowa, NJ, 2000) pp. 1–16.
- [52] L. Weber, A. Honecker, B. Normand, P. Corboz, F. Mila, and S. Wessel, Quantum Monte Carlo simulations in the trimer basis: first-order transitions and thermal critical points in frustrated trilayer magnets, *SciPost Phys.* **12**, 054 (2022).
- [53] J. Luo, L. Xu, E. Lascaris, H. E. Stanley, and S. V. Buldyrev, Behavior of the widom line in critical phenomena, *Phys. Rev. Lett.* **112**, 135701 (2014).
- [54] N. A. de Oliveira, P. J. von Ranke, and A. Troper, Magnetocaloric and barocaloric effects: Theoretical description and trends, *Int. J. Refrig* **37**, 237 (2014).
- [55] P. J. Shirron, Applications of the magnetocaloric effect in single-stage, multi-stage and continuous adiabatic demagnetization refrigerators, *Cryogenics* **62**, 130 (2014).
- [56] A. E. Jahromi, P. J. Shirron, and M. J. DiPirro, *Sub-Kelvin Cooling Systems for Quantum Computers*, Tech. Rep. (NASA Goddard Space Flight Center Greenbelt, MD, United States, 2019).
- [57] Q. Li, Y. Gao, Y.-Y. He, Y. Qi, B.-B. Chen, and W. Li, Tangent space approach for thermal tensor network simulations of 2D Hubbard model, [2212.11973v1](#).
- [58] Yuan Gao, Qiaoyi Li, Junsen Wang, Han Li, Bin-Bin Chen and Wei Li, in preparation.
- [59] E. M. Stoudenmire and S. R. White, Studying two-dimensional systems with the density matrix renormalization group, *Annu. Rev. Condens. Matter Phys.* **3**, 111 (2012).
- [60] A. Weichselbaum, Non-abelian symmetries in tensor networks: A quantum symmetry space approach, *Ann. Phys.* **327**, 2972 (2012).
- [61] A. Weichselbaum, X-symbols for non-Abelian symmetries in tensor networks, *Phys. Rev. Res.* **2**, 023385 (2020).
- [62] Y.-L. Dong, L. Chen, Y.-J. Liu, and W. Li, Bilayer linearized tensor renormalization group approach for thermal tensor networks, *Phys. Rev. B* **95**, 144428 (2017).
- [63] L. Zhu, M. Garst, A. Rosch, and Q. Si, Universally diverging Grüneisen parameter and the magnetocaloric effect close to quantum critical points, *Phys. Rev. Lett.* **91**, 066404 (2003).
- [64] M. Garst and A. Rosch, Sign change of the Grüneisen parameter and magnetocaloric effect near quantum critical points, *Phys. Rev. B* **72**, 205129 (2005).

Supplemental Material

Junsen Wang, Han Li, Ning Xi, Yuan Gao, Qing-Bo Yan, Wei Li, and Gang Su

I. FINITE-TEMPERATURE TENSOR RENORMALIZATION GROUP

Here we present more details of the thermal tensor network approaches employed in the present study of Shastry-Sutherland (SS) model, i.e., the exponential tensor renormalization group (XTRG) based on matrix product operators (MPOs). XTRG is a highly controllable method that can reach low temperature exponentially fast. Starting with a quasi-1D mapping of the original square lattice into a snake path, we represent the Hamiltonian H in the form of an MPO. At a very high temperature $\beta_0 \equiv 1/T_0 \ll 1$, the density matrix $\rho_0(\beta_0)$ of the system can be expanded as [40],

$$\rho_0(\beta_0) \simeq \sum_{n=0}^{n_c} \frac{(-1)^n \beta_0^n}{n!} H^n, \quad (\text{S1})$$

with n_c a small integer (less than 10 in practice). For example, when $\beta_0 = 10^{-6}$, $n_c = 3$ suffices to result in very accurate representation essentially free of expansion error. After that, we keep squaring the MPO [41]

$$\rho_m(2^m \beta_0) = \rho_{m-1}(2^{m-1} \beta_0) \cdot \rho_{m-1}(2^{m-1} \beta_0), \quad (\text{S2})$$

and the system cools down exponentially fast. As the MPO product in Eq. (S2) leads to enlarged bond dimension, one actually needs to compress the bond space. Naively, the numerical cost for the MPO compression scales like $\mathcal{O}(D^6)$. However, a $\mathcal{O}(D^4)$ complexity can be achieved with a variational optimization [40]. To retain even larger bond dimension, a new method dubbed *tanTRG* with $\mathcal{O}(D^3)$ complexity has been developed very recently to tackle the challenging problem like 2D Hubbard model [57]. Details and more elaborative examples on this method applied to quantum spin systems will be described in a separate work [58].

As illustrated in Fig. 1(a), the SS model is put on a $W \times L$ cylindrical lattice with W being the width and L the length. To relieve severe boundary effects, instead of the standard $L/W = 2$ aspect ratio [25, 59], we stick to a larger one, $L/W = 4$ with fixed width $W = 6$, and the simulations are performed down to a very low temperature of $T/J' \sim 0.006$. In zero (nonzero) magnetic field, the global spin SU(2) [U(1)] symmetry of the MPO is exploited based on the QSpace tensor library [60, 61]. The calculations are performed by retaining up to $D^* = 2000$ multiplets, equivalent to $D \approx 6000$ U(1) states. In practice, we

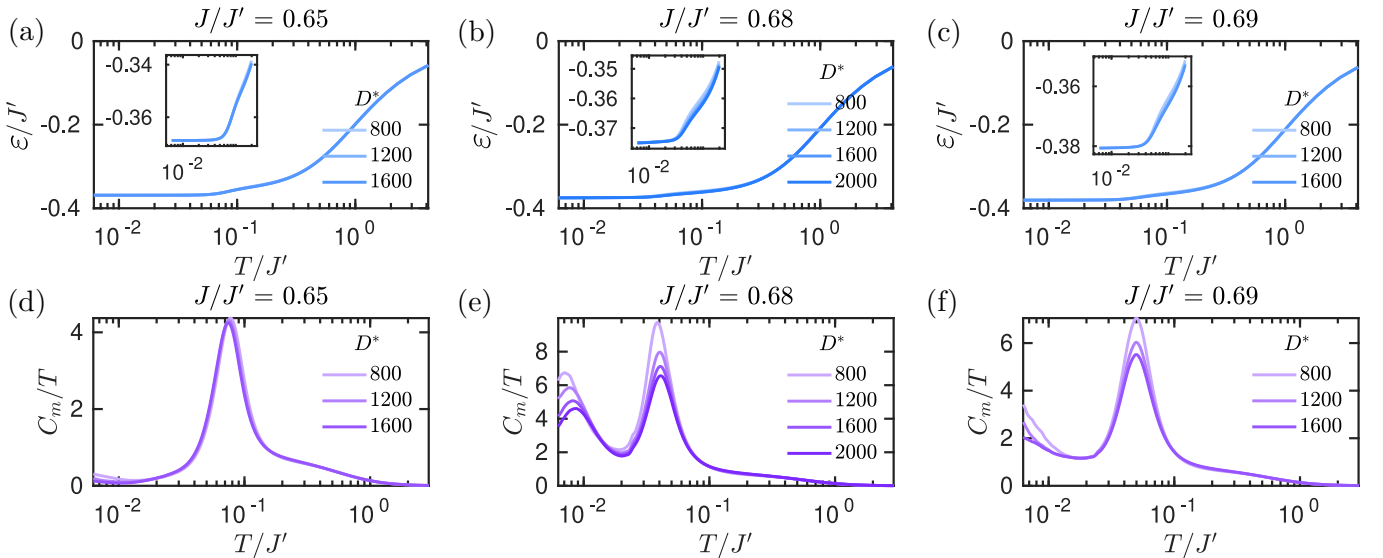


FIG. S1. Convergence of the thermal tensor network simulation results for (a-c) internal energy per site $\varepsilon = \langle H \rangle_\beta / N$ and (d-f) magnetic specific heat C_m/T . Insets in the first row zoom in into the low-temperature results.

always firstly ramp up β exponentially, then followed by either an exponential increase using XTRG, or a linear increase using *tan*TRG. Along the way, utilizing a bilayer tensor trace [62], all thermodynamic quantities can be obtained with high accuracy.

In Fig. S1, we show the internal energy per site $\varepsilon = \langle H \rangle_\beta / N$ and magnetic specific heat C_m/T for several different bond dimensions D^* . It is found that the convergence is well reached for $D^* = 1600$ or 2000 (for more challenging case near the DS-PS transition), which is used in our numerical results presented in the main text.

II. DENSITY MATRIX RENORMALIZATION GROUP SIMULATIONS

In this section, we show the ground-state density matrix renormalization group (DMRG) calculations of the Shastry-Sutherland (SS) model under both zero and finite fields as a complement to the thermal tensor renormalization group results.

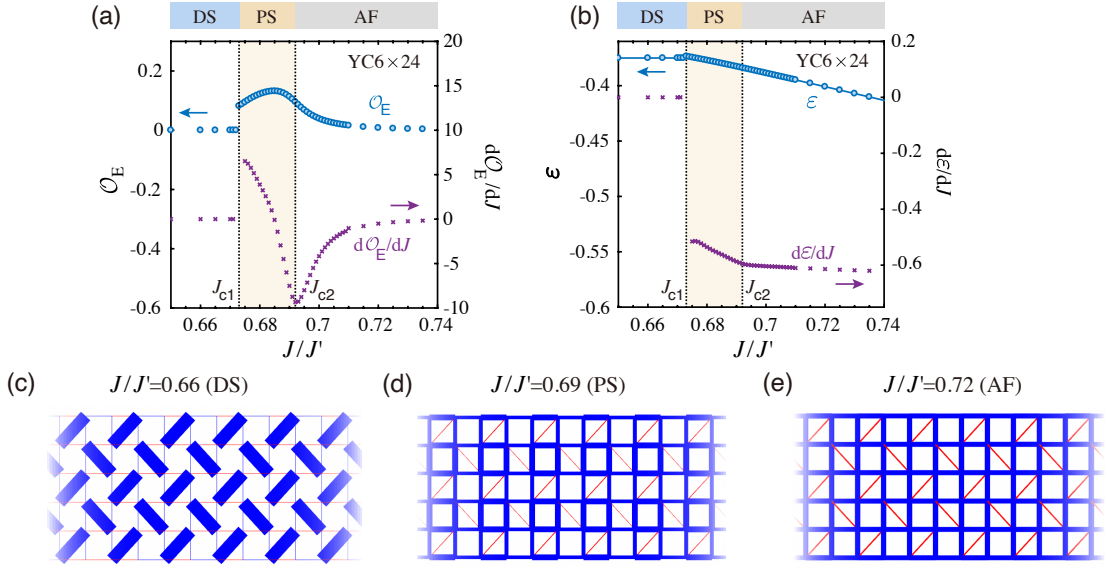


FIG. S2. Pressure-driven quantum phase transitions in the SS model simulated on a 6×24 cylinder. (a) shows the PS order parameter \mathcal{O}_E and its derivatives $d\mathcal{O}_E/dJ$, where two QPTs separating the DS, PS, and AF phases can be observed at $J_{c1} \simeq 0.673$ and $J_{c2} \simeq 0.692$, respectively. (b) shows the ground-state energy per site ε and its derivatives $d\varepsilon/dJ$ averaged over the central four sites of the lattice, where $d\varepsilon/dJ$ is found to be continuous and shows a kink at J_{c2} . (c-e) illustrate the three phases at representative coupling parameters, where the widths of the blue (red) bond indicate the negative (positive) values of the spin-spin correlations $\langle S_i S_j \rangle$.

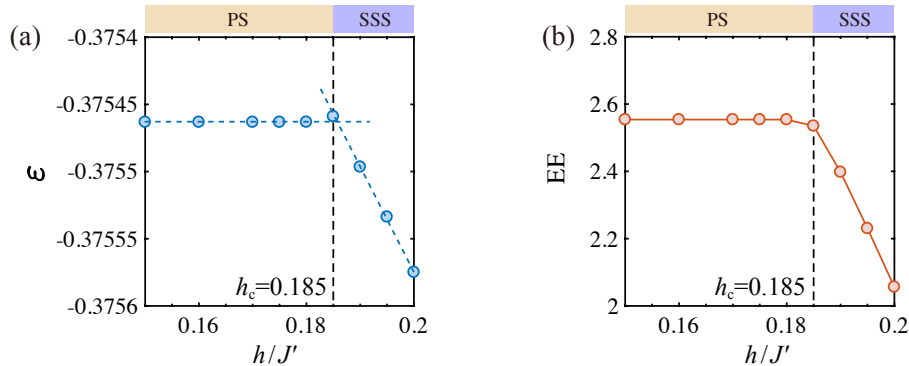


FIG. S3. The ground state energy per site ε and entanglement entropy (EE) of SS model under magnetic fields. The calculations are performed on a 6×30 cylinder with $D = 1024$, where we fix $J/J' = 0.68$. In (a), the energy per site ε shows a kink at $h_c \simeq 0.185$, and in (b) the EE starts to decrease at $h_c \simeq 0.185$ and there is no divergence can be observed. The results indicate that the QPT between the plaquette singlet (PS) and SSS phases is of first order.

Two quantum phase transitions of SS model at zero fields.— In Fig. S2, we calculate the empty plaquette singlet (PS) order

parameter \mathcal{O}_E , the ground-state energy $\varepsilon \equiv E/N_{\text{central}}$ average over central sites of the lattice, and their derivatives to determine the quantum phase transition (QPT), where the simulations are performed on the $W \times L$ cylinder with width $W = 6$ and length $L = 24$. The kept bond dimension D^* is up to 1024 multiplets, with SU(2) symmetry implemented [60, 61], and the small truncation errors (below $\sim 10^{-7}$) guarantee high accuracies. During the calculations, the intra-dimer Heisenberg coupling is fixed as $J' = 1$, and the NN coupling J is varied in the calculations, controlling the ratio $\alpha \equiv J/J'$. As shown in Fig. S2(a), two QPTs from the dimer singlet (DS) [illustrated in Fig. S2(c)] to the PS phase [c.f., Fig. S2(d)] and then to antiferromagnetic (AF) states [Fig. S2(e)] can be clearly identified, which are labelled as J_{c1} and J_{c2} , respectively. For small J values, the system is in the DS phase [c.f. Fig. S2(c)], and as J is increased, the nonzero \mathcal{O}_E witnesses the abrupt rise of the PS order. In Fig. S2(a), we find \mathcal{O}_E shows a sudden jump at $J_{c1} \simeq 0.673$. Such discontinuity is also seen for ε as shown in Fig. S2(b), indicating that the QPT at J_{c1} is of first-order.

Further increasing J , the values of \mathcal{O}_E gradually decrease as the system leaves the PS phase and enters the AF phase, where a dip in $d\mathcal{O}_E/dJ$ appears at about $J_{c2} \simeq 0.692$, i.e., the order parameter decreases most rapidly at around J_{c2} . This PS-AF QPT can also be seen in the results of energy per site ε , whose first-order derivative is found to be continuous in Fig. S2(b). There also exists a kink in $d\varepsilon/dJ$ at $J_{c2} \simeq 0.692$, which also clearly locates the second-order PS-AF transition.

The spin supersolid transition.— There are rich field-induced quantum spin states in SS model under magnetic fields [33]. Here in Fig. S3, for a typical $J = 0.68$, we perform DMRG calculations on $YC6 \times 30$ lattices and keep $D = 1024$ states (with small truncation error $\sim 10^{-5}$) and find the field-induced spin supersolid transition occurs at $h_c \simeq 0.185J'$. At small magnetic fields $h < h_c$, the system resides in the PS phase, where all the local moments $\langle M_\gamma \rangle$ ($\gamma = x, y, z$) equal zero, as discussed in the main text. By increasing h , we find the system enters a spin supersolid (SSS) phase at h_c . In Fig. S3(a) and (b), the energy per site ε and entanglement entropy (EE) curves are shown, respectively, where the kink in energy and absence of divergence in EE results can be clearly observed at h_c , indicating that the QPT is of first-order.

III. MORE RESULTS ON THE SS MODEL AT ZERO MAGNETIC FIELD

A. Details on magnetic specific heat data

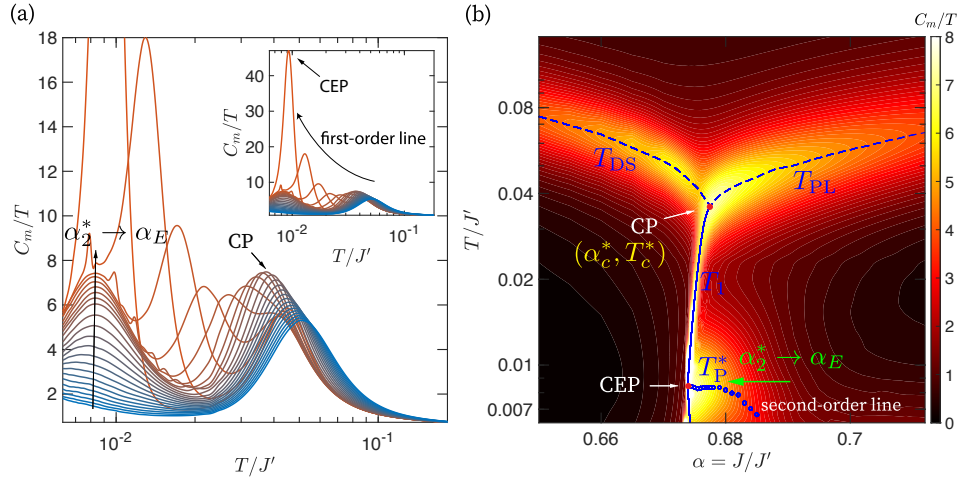


FIG. S4. (a) Magnetic specific heat C_m/T v.s. temperature T/J' , for the coupling ratio α ranging from $\alpha_2^* \simeq 0.692$ to $\alpha_E = 0.674$. (b) Contour plot of magnetic specific heat C_m/T . The CP and CEP represent the critical point and critical endpoint of second-order phase transitions, respectively.

Here we discuss in more details on magnetic specific heat data. In Fig. S4(a), we show C_m/T v.s. T/J' , for the coupling ratio α ranging from α_2^* (PS-AF transition point) to α_E (critical endpoint). As α decreases, the high- T hump (i.e., T_{PL}) evolves into a peak labeled by the critical point (CP) around $T/J' \sim 0.04$ at $\alpha = \alpha_c^*$. Further decreasing α , this peak shifts to lower temperature (i.e., T_1) and becomes more pronounced. It eventually evolves into the critical endpoint (CEP) at α_E . On the other hand, there is always a low- T peak around $T/J' \sim 0.008$ (i.e., T_P^*), which almost remains as a constant for α close to α_E . Moreover, for $\alpha < \alpha_c^*$, an additional hump emerges at a temperature T/J' higher than 0.04 (i.e., T_{DS}). We note that there are satellite subpeaks for α close to α_E , which are artifacts due to numerical errors, reflecting the fact that specific heat calculations are rather challenging at such low temperature. In Fig. S4(b), we show the contour plot of the magnetic specific heat C_m/T in

a larger size and cleaner manner [as compared to Fig. 1(a) in the main text]. The blue circles at the T_P^* line, corresponding to peaks of C_m/T , are numerical data obtained in our calculation.

B. Empty and full plaquette singlet order parameters

Here we examine the full PS order parameter \mathcal{O}_F and compare with the behavior of empty PS order parameter, \mathcal{O}_E , which is discussed in the main text. Note that their definitions are indicated in the inset of Fig. 2(c) and Fig. S6(a).

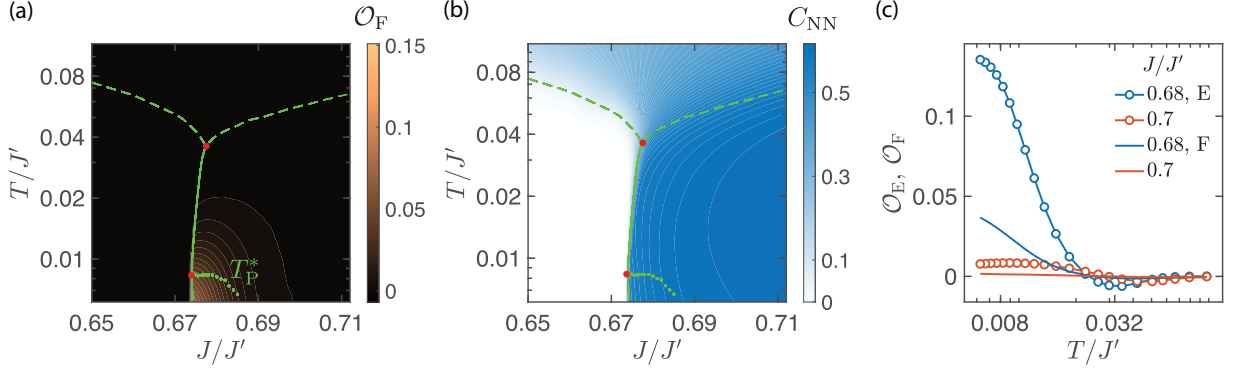


FIG. S5. Contour plots of (a) full PS order parameter \mathcal{O}_F , and (b) inter-dimer correlator C_{NN} . Scale of the colorbar in (a) is the same as that used in Fig. 2(b) of the main text. Green dashed, solid and dotted lines are peaks of C_m/T , two red points are CP and CEP, respectively [c.f. Fig. 1(a)]. (c) Temperature dependence of order parameters \mathcal{O}_E , \mathcal{O}_F for both empty and full PS states, respectively.

Before presenting numerical results, we firstly explain how to obtain these order parameters in practice. Due to the underlying snake path geometry for the MPO used, horizontal bonds have a tendency to be weaker than vertical bonds. As illustrated in Fig. 1(c) of the main text, this is due to the fact that vertical bonds are long-ranged ones while horizontal bonds are usually nearest neighboring. Moreover, due to the cylindrical geometry used, boundary effects can induce a particular empty PS pattern near the boundaries [25]. In practice, we sum both two horizontal bonds and two vertical bonds emanating from each of the four sublattices of the *central* unit cell, with appropriate signs taken into account as illustrated in the inset of Fig. S6(a).

In Fig. S5(a), we show the corresponding contour plot of the \mathbb{Z}_2 symmetry breaking order parameter for full PS, and compare the results to Fig. 2(b) in the main text. It clearly shows that \mathcal{O}_F remains zero until the temperature decreases also to T_P^* . Moreover, below this temperature scale, \mathcal{O}_F is much smaller than \mathcal{O}_E , which indicates that the empty plaquette indeed wins the competition in the \mathbb{Z}_2 symmetry breaking order. In Fig. S5(c), we compare the temperature evolution of \mathcal{O}_E and \mathcal{O}_F , and find indeed the former is larger than the latter at low temperature in the PS phase. On the other hand, in the AF phase both parameters remain small till the lowest temperature.

As a sidenote, we also present the contour plot of the inter-dimer correlator C_{NN} in Fig. S5(b), which shows that it becomes nonzero outside the DS phase. This complementary behaviors in comparison with the intra-dimer correlator C_D given in Fig. 2(a) of the main text confirm the nature of the first-order DS-PS phase transition.

C. Plaquette singlet susceptibility

To resolve the issue that whether the \mathbb{Z}_2 symmetry breaking occurs among the empty or full plaquettes, here we reveal their competitions across the full temperature windows. Namely, we calculate PS susceptibility for both empty and full PS orders, defined by $\chi_P = [\mathcal{O}_P(\delta J_P) - \mathcal{O}_P(0)]/\delta J_P$, with $P = E$ or F . Here δJ_P means a small “pinning field” for inter-dimer coupling $J \rightarrow J \pm \delta J_P$, as shown in the inset of Fig. S6(a). In Fig. S6(a), we present two types of PS susceptibility for $\alpha = 0.68$. It clearly shows that χ_E is larger than χ_F even for relatively high temperatures. Moreover, the former increases much faster than the latter in the PL regime below T_{PL} , and reaches its maximal value around T_P^* , indicating the occurrence of \mathbb{Z}_2 symmetry breaking there. Therefore, we conclude that the empty PS instability predominates over the full one in the low-temperature regime in the temperature-pressure phase diagram. Moreover, although the full PS susceptibility is relatively small, it is nonzero and indicates the existence of a competition that may be responsible for the very low PS order transition temperature. Symmetry breaking eventually occurs at T_P^* , which is two orders of magnitude smaller than the coupling strength of the model, a manifestation of PS order competition and strong spin fluctuations.

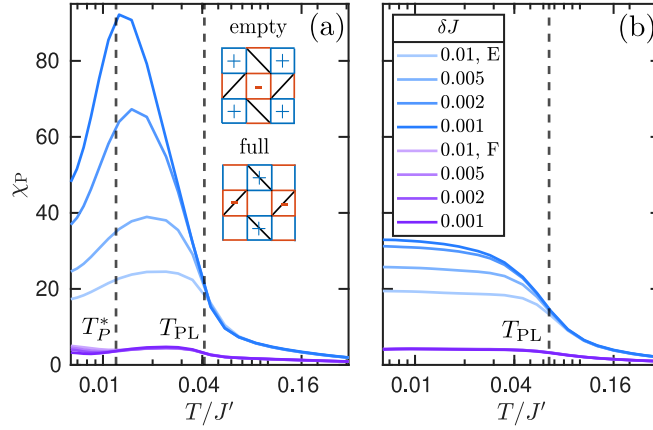


FIG. S6. PS susceptibility χ_P at (a) $J/J' = 0.68$ and (b) $J/J' = 0.71$, for empty ($P = E$) and full ($P = F$) PS order parameters, and illustrated in inset of the left figure. Four different values of δJ are used to ensure convergence of χ_P calculations.

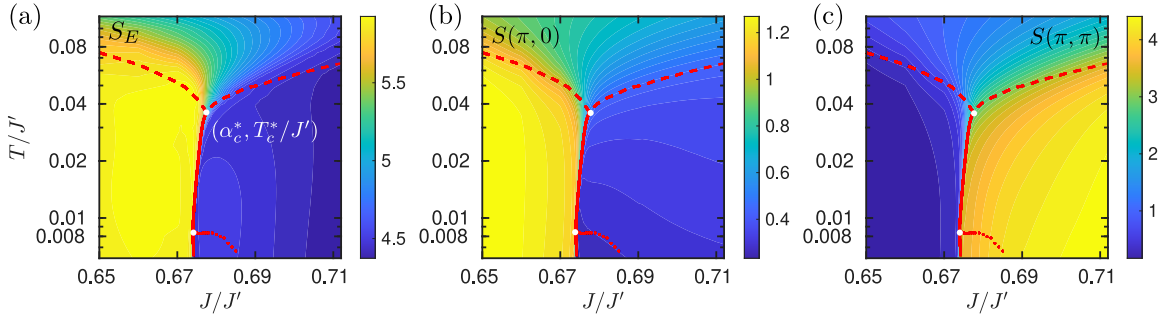


FIG. S7. Contour plots of (a) the MPO EE S_E , (b) static spin structure factor $S(\pi, 0)$ and (c) $S(\pi, \pi)$. The red dashed, solid and dotted lines are determined from the peaks of C_m/T , and the two white dots represent the CP and CEP, respectively.

In Fig. S6(b), the same quantities are plotted for $\alpha = 0.71$. We find again that χ_E increases much faster than χ_F for $T \lesssim T_{PL}$. However, this increase soon saturates to a constant value as the temperature further decreases. It indicates that the \mathbb{Z}_2 symmetry breaking order has never been built up for this case, and the two types of PS correlations remain fluctuating. Indeed, the ground state for this case is the AF Néel state as obtained by DMRG (c.f. Sec. II).

D. Pressure-induced phase transitions in the SS model

In this subsection, we provide more evidence on the DS-PS (and DS to the plaquette-single liquid, PL) phase transitions, and in the end also discuss the mysterious PS-AF phase transition from our finite- T data. Note the intra-dimer correlator, C_D , is used in the main text to reveal the existence of the first-order transition line.

MPO entanglement entropy.— Taking an MPO as a supervector, a Schmidt decomposition of this purified wavefunction can be performed and the entanglement entropy (EE) S_E between the two parts of the system can be computed. Here we divided the density matrix MPO at the middle bond and compute the corresponding MPO EE in Fig. S7. It shows that the DS phase has larger values than other phases, and there is a jump at the first-order transition line. At higher temperatures, MPO entanglement entropy instead exhibits a smooth crossover as tuning J/J' .

Static spin structure factor.— Another interesting quantity to characterize the spin states and transitions is the static spin structure factor $S(\mathbf{k}) = N^{-1} \sum_{i,j} e^{-i\mathbf{k} \cdot (\mathbf{r}_i - \mathbf{r}_j)} \langle \mathbf{S}_i \cdot \mathbf{S}_j \rangle$, where N is the total lattice sites and $\mathbf{k} = [k_x, k_y]$. A particular temperature evolution of this quantity is given in the second column of Fig. 1(c) for $J/J' = 0.676$. Here we focus on the two particular momentum points, $\mathbf{k} = (\pi, 0)$ and $\mathbf{k} = (\pi, \pi)$. The DS phase has a structure peak at $(\pi, 0)$, while the other phases of this model exhibits peak at (π, π) [14]. Contour plots of these two quantities are shown in Fig. S7(b) and (c). Indeed in Fig. S7(b) we see that in the DS phase, the $S(\pi, 0)$ takes the larger values than those of PL, PS, and AF phases; while the case is reversed in Fig. S7(c). The first-order line again is evident by a jump for $T < T_c^*$ as J/J' varies; while they can changes smoothly for higher temperatures above T_c^* .

On the PS-AF transition.— According to the ground-state DMRG calculations, a phase possesses long-range AF order appears for high pressure (c.f., Sec. II). It follows that there must exist a QPT between the empty PS and AF phases in the SS model. From the specific heat and correlation results in Figs. 1 and 2 of the main text, a typical first-order transition is ruled out and they point to a possible existence of QCP there. However, all quantities calculated at finite temperature in this work show no clear evidence for the putative PS-AF phase transition. This can be due to the fact that this transition is a very weak one as proposed in Ref. [18, 22] and the relevant temperature scale is extremely low and out of reach from our numerics. At present we are not able to determine the nature of this QPT, nevertheless, our study indicates that this phase transition may be equally hard to detect experimentally even down to low temperature.

E. Critical scaling in order parameter C_D

As shown in Fig. 2(a) of the main text, the intra-dimer correlator $C_D \equiv -\langle \mathbf{S}_i \cdot \mathbf{S}_j \rangle_D$, for sites i and j belonging to a diagonal dimer J' bond, serves as the order parameter detecting the first-order transition of DS-PL. Namely, for the DS (PL) phase, C_D is positive (negative). In this sense, it plays the role of density-type order parameter as in water's phase diagram for distinguishing the liquid and gas phases. Since the difference is defined not by a change in symmetry, but by a scalar which takes two different values at the discontinuity, the corresponding critical point belongs to the 2D Ising universality class. here we confirm this argument by studying the critical scaling behavior of C_D .

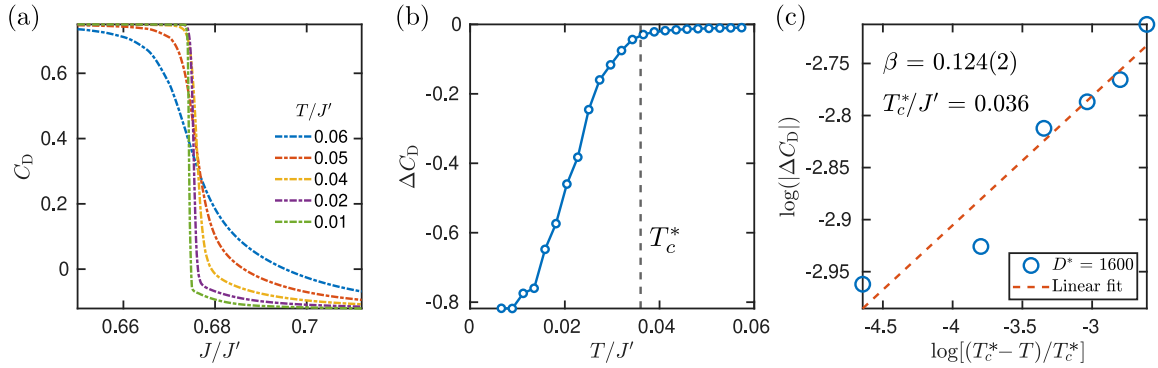


FIG. S8. (a) Dimer correlator C_D as a function of J/J' . (b) Discontinuity of dimer correlator, ΔC_D , at the first-order transition line, is plotted as a function of temperature. (c) Log-log plot of the ΔC_D v.s. the reduced temperature, from which an exponent of $\beta \simeq 1/8$ can be extracted that agrees with 2D Ising universality class.

In Fig. S8(a), we show C_D as a function of J/J' for several different temperatures. It is found that there is indeed a abrupt jump in C_D for low temperatures, while the change becomes smooth at higher temperatures. We extract this jump in C_D at the first-order transition line, ΔC_D , show the results in Fig. S8(b) as a function of T . We find ΔC_D decreases monotonically as the temperature increases and vanishes when approaching T_c^* .

Location of the critical point is determined as the crossing point between three lines determined from the peaks of C_m/T as shown in Fig. 1(a), which gives $(\alpha_c^*, T_c^*/J') = (0.678, 0.036)$. We then define the reduced temperature $\tilde{t} = (T_c^* - T)/T_c^*$, and the discontinuity ΔC_D as a function of \tilde{t} is shown in Fig. S8(c) in a log-log scale. Through a linear fit, we extract the critical exponent β from $|\Delta C_D| = \tilde{t}^\beta$, which leads to $\beta \approx 0.124$, in agreement with the 2D Ising exponent $\beta = 1/8$.

F. Temperature derivatives of the intra- and inter-dimer singlet correlators

Two types of local correlations, intra-dimer C_D and inter-dimer C_{NN} , play a central role in characterizing the finite- T phases of the SS model. As shown by Fig. 2(a) in the main text and Fig. S5(b) above, C_D (C_{NN}) dominates in the DS (PS) phase, respectively. It is thus important to further investigate their temperature evolution. In particular, one straightforward quantity is their partial derivative with respect to temperature T , which has a clear physical meaning: $\gamma_P = -(\partial S/\partial P)_T \sim \partial(\mathcal{A}C_D + \mathcal{B}C_{NN})/\partial T$ (with \mathcal{A}, \mathcal{B} material-dependent coefficients) characterizes the magnetic barocaloric effect.

In Fig. S9(a) and (b), we show the temperature derivatives of these two local correlators. It is found that near the critical point there are two white dashed lines forming local extrema, analogous to the peaks of C_m/T (indicated by the green dashed

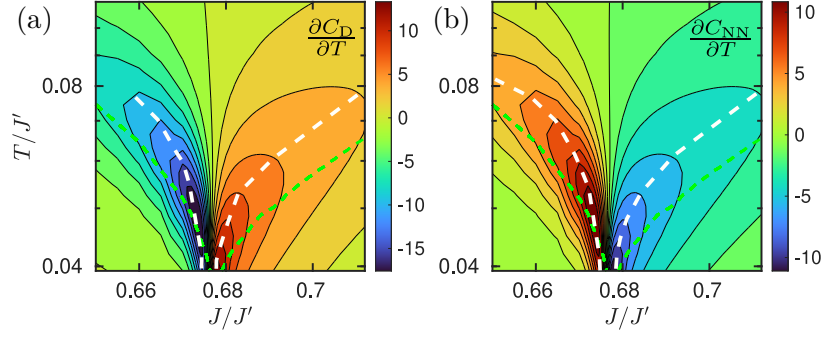


FIG. S9. Partial derivative of (a) intra-dimer correlator C_D and (b) inter-dimer correlator C_{NN} with respect to temperature T (under fixed pressure P). The green dashed lines are peaks of C_m/T [c.f. Fig. 1(b) of the main text]. The white dashed lines connects the extrema (peaks or dips) of the contour lines.

lines). The derivatives are found to have different sign in the DS and PL/PS regimes, and the peak values increase as temperature decrease.

IV. MORE RESULTS ON THE SS MODEL IN FINITE MAGNETIC FIELDS

A. Magnetocaloric evidence for the spin supersolid transition

In the main text, we find the magnetic specific heat C_m/T exhibits certain signatures of the PS-SSS QPT. Here we present more clear evidences in terms of magnetocaloric responses.

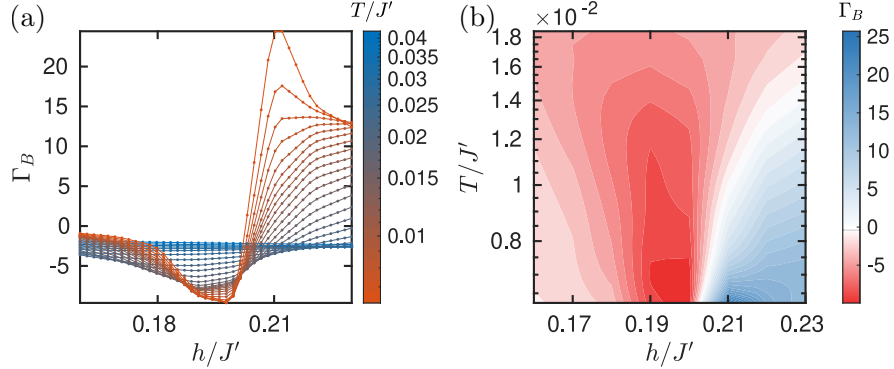


FIG. S10. (a) Magnetic Grüneisen ratio Γ_B as a function of h/J' for different low temperatures, and (b) the corresponding contour plot. The results are obtained for $J/J' = 0.68$ with $D = 3200$ U(1) states retained in the simulations.

In Fig. S10, we show the computed magnetic Grüneisen ratio, defined by $\Gamma_B = -\frac{1}{T} \frac{(\partial S / \partial h)_T}{(\partial S / \partial T)_h}$, as a function of the external magnetic field h/J' , for different temperatures. The thermal entropy results are obtained with $D = 3200$ U(1) states. It is found that Γ_B indeed tends to diverge near the QPT with a sign change at low T [63, 64], which are shown in the Γ_B vs. fields h in Fig. S10(a) and the corresponding contour plot in Fig. S10(b). We note that this prominent magnetocaloric response can be used to probe the SSS transition experimentally from magnetocaloric measurements.

B. Temperature evolution of the spin structure factors

Here we discuss nature of the state sitting on the right bottom corner of Fig. 4(a) in the main text, where a new phase different from the high-temperature PL phase is expected. As revealed by the DMRG calculations elaborated in Sec. II, the ground state corresponds to an intriguing 10×2 stripy SSS phase, where both the discrete translational symmetry (diagonal “solid” order) and the spin rotation symmetry along z axis (off-diagonal “superfluid” order) are spontaneously broken. As temperature ramps

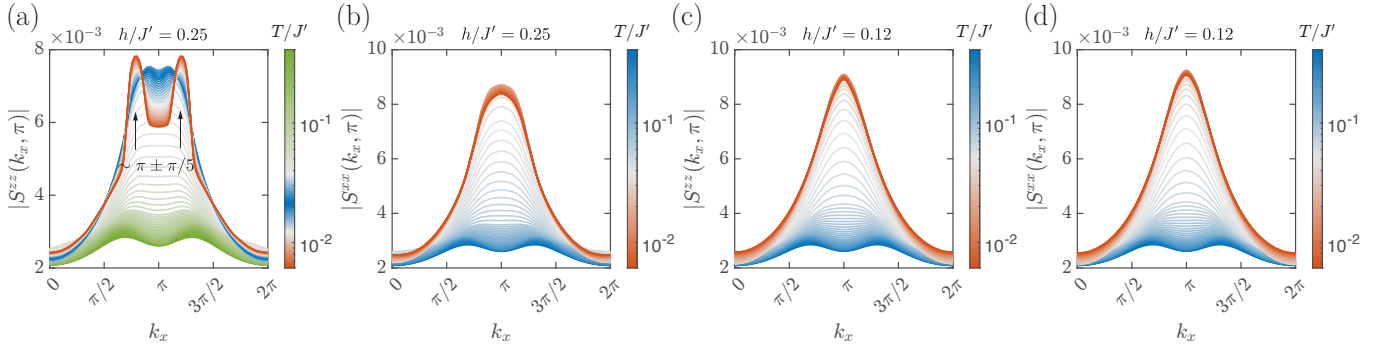


FIG. S11. Spin structure factors $S^{zz}(k_x, k_y)$ (a,c) and $S^{xx}(k_x, k_y)$ (b,d), plotted along the lines with fixed $k_y = \pi$.

up, there are in principle three possibilities for the broken symmetries to restore: either the discrete or continuous symmetry firstly restores, or they occur at the same temperature (which is not very likely though).

To verify which scenario happens in the SS model for $J/J' = 0.68$, we consider the spin structure factors in the spin z and x components defined as

$$S^{\gamma\gamma}(\mathbf{k}) = \frac{1}{N} \sum_{i,j} e^{i\mathbf{k} \cdot (\mathbf{r}_i - \mathbf{r}_j)} \langle S_i^\gamma S_j^\gamma \rangle, \quad \text{for } \gamma = x, y, z. \quad (\text{S3})$$

In the PS phase, both $S^{xx}(\mathbf{k})$ and $S^{zz}(\mathbf{k})$ should peak at $\mathbf{k} = M = (\pi, \pi)$ [14]; while in the SSS phase, we expect that both of them exhibit peaks at $(\pi \pm \pi/5, \pi)$, since the discrete symmetry breaking pattern is 10×2 , as illustrated explicitly in Fig. 4(c) of the main text.

In Fig. S11, we fix $k_y = \pi$ and show the temperature evolutions of spin structure factors. It is found that for $h/J' = 0.25$, the peak of S^{zz} firstly develops around M for temperature reaching T_{PL} , then it shifts to other two symmetric momenta as temperature further lowers, suggesting a discrete symmetry breaking of the system in this temperature regime [c.f. Fig. S11(a)]. On the other hand, the peak of S^{xx} remains at M down to the lowest accessible temperature [c.f. Fig. S11(b)]. It is likely that the BKT temperature is with an even lower value out of reach by our finite-temperature calculations. As a comparison, we also show the case with $h/J' = 0.12$ (in the PS phase), where it is found that both components establish clear peaks at M without any splitting, for temperatures below T_{PL} [c.f. Fig. S11(c-d)]. We also note that this peak is sharper for $h/J' = 0.12$ than those of $h/J' = 0.25$ case. We note that these temperature evolution of spin structure factors can be experimentally detected via neutron scattering experiments, and provide experimental evidence for the spin supersolid phase in $\text{SrCu}_2(\text{BO}_3)_2$ under finite magnetic fields.